Beyond Crease Geometry: Multistability in Origami-Inspired Structures through Local Fold Architectures

Sagi Senderovich[a], Ezra Ben-Abu[a], Shai Elbaz[a], Nadav Zemah[a], Anna Zigelman[a], and Amir D. Gat[a,2]

Origami-inspired tubular structures provide a versatile platform for shape morphing, with multistability achieved predominantly through crease-network geometry. Expanding the range of morphing behaviors can therefore require increasingly intricate crease patterns that become more difficult to model and fabricate, ultimately constraining the realizable morphing landscape. Here, we expand the design space of origami-inspired structures beyond geometry by introducing localized instabilities within the crease network, thereby creating compliant multistable structures whose local fold architectures govern global deformation and stability through both constitutive mechanics and geometric constraints. To relate local fold architectures to global multistability, we develop and experimentally validate a modeling framework in which compliant folds are represented as continuous fields that capture spatially varying bistable mechanics. Force- and displacement-controlled design maps demonstrate that global deformation and stability can be programmed through the fold architecture's local parameters. Redistributing bistability within a fixed crease-network topology shifts the global response between compliant, spatially distributed deformation in semi-bistable architectures and discrete transitions within a hierarchically organized space of stable configurations in fully bistable architectures. These results establish a local-to-global design principle for programming both the stable configurations of a structure and the transition pathways connecting them, expanding the design space for multistable metamaterials, adaptive morphing structures, and soft robotic systems.

Multistable origami | origami tubes | deployable structures | reconfigurable metamaterials

Significance

Conventional origami relies predominantly on crease-network geometry to program multistability, linking broader morphing capabilities to greater geometric complexity. We show that another design dimension lies in the nonlinear mechanics of the folds themselves. As a result, local fold parameters govern global deformation and stability, while redistributing bistability within the same crease network shifts global behavior between compliant, spatially distributed phase transformation and discrete switching among hierarchically organized stable configurations. This demonstrates that local fold architecture can determine not only which shapes a structure retains, but also how it moves between them. This local-to-global design principle expands the design space for multistable metamaterials, adaptive structures, and soft robotic systems.

Multistable structures possess multiple stable states separated by energy barriers, allowing them to retain distinct configurations without continuous energy input. Under external actuation, transitions between such states proceed through unstable regions via snap-through events (1–3). These features enable robust and programmable shape morphing, a capability often leveraged in adaptive systems (4–6), soft robotic actuators (7–11), and metamaterials (12–14).

One prominent route to realizing such programmable multistability is origami-inspired design, in which global deformation emerges from the coupled mechanics and geometry of interconnected facets and creases. The stiffnesses of these facets and creases determine the energetic cost of deformation, while the geometry of the crease network imposes compatibility constraints on the admissible deformation modes (15–17). A prominent tubular example is the Kresling pattern, in which a triangulated cylindrical crease network couples axial displacement and twist (18, 19).

Author affiliations: [a]Faculty of Mechanical Engineering, Technion–Israel Institute of Technology, Haifa 3200003, Israel

The authors declare no conflict of interest.

[2]To whom correspondence should be addressed. E-mail: amirgat@technion.ac.il

In conventional origami architectures, however, facets and creases typically provide either rigid constraints or locally monostable compliance, such that global multistability emerges primarily from compatibility constraints associated with crease-network geometry (20–23). Consequently, expanding the range of morphing behaviors often requires increasingly intricate crease patterns that become more difficult to model and fabricate, ultimately constraining the realizable morphing landscape.

To overcome this limitation, we expand the origami design space by embedding local bistability within compliant crease networks through shell inversion (24, 25), thereby introducing fold architectures that govern global deformation and stability through both local nonlinear mechanics and geometric constraints. We refer to the resulting class of tubular structures as Mixed Folded Tubes (MFTs).

This structural concept motivates an examination of how local nonlinear fold mechanics shape the global structural response and how they can be modeled efficiently and robustly for systematic design. Doing so requires a predictive formulation that treats spatially varying fold geometry and nonlinear fold constitutive behavior as design variables governing the global response. Although the finite element method (FEM) and the reduced-order bar-and-hinge (B&H) formulations have been used to model the multistable mechanics of compliant shell structures (26–28), their systematic application to folding architectures with interacting deformation modes and spatially varying nonlinear mechanics can be computationally intensive and numerically challenging. FEM analyses can become computationally expensive and sensitive to convergence near instabilities, whereas B&H models require detailed facet-and-hinge discretizations and constitutive calibration of the compliant folds. These limitations motivate BiPlan, a specialized formulation that represents fold extension through continuous fields that capture spatially varying bistable mechanics as the dominant deformation mechanism, thereby relating the local mechanics of the fold architecture to global deformation and stability.

Using BiPlan together with experiments, we compare semi-bistable and fully bistable fold architectures that share a common crease-network topology but differ in the distribution of local bistability. This controlled comparison isolates the influence of local constitutive behavior from that of the underlying geometric constraints and reveals how the distribution of local bistability governs global deformation, stability, and the transition pathways connecting stable configurations.

For the semi-bistable architecture, force- and displacement-controlled design maps demonstrate how global deformation and stability can be programmed through local geometric and constitutive parameters. In the fully bistable architecture, interacting bistable folds produce discrete transition pathways within a hierarchically organized space of stable configurations. The two architectures therefore exhibit complementary mechanical behaviors, ranging from compliant, spatially distributed phase transformations in the semi-bistable MFT to discrete transitions between stable configurations in the fully bistable MFT. Together, these results establish local fold architecture as a design strategy for programming both the stable shapes of a structure and the transition pathways connecting them, positioning MFTs as a versatile platform for multistable metamaterials, adaptive morphing structures, and soft robotic systems.

MFT Fold Architectures: Geometry and Local Mechanics

We consider two MFT variants with a common crease-network topology comprising intersecting helical and circular fold sets embedded in a tubular shell (Fig. 1.E). Each variant's fold architecture is defined by the geometry of this crease network together with the constitutive response assigned to each fold set. The crease-network geometry constrains the admissible deformation modes and modulates their geometric coupling. Increasing the circular-fold pitch produces a wider helical pattern with greater axial resistance, whereas decreasing the helical-fold angle produces a narrower pattern with stronger axial–transverse coupling (Fig. 1.A). The constitutive response assigned to each fold set then shapes the energetic landscape over this geometry-constrained deformation space.

The first variant employs a semi-bistable fold architecture (Fig. 1.A–B) realized through plasticity-induced shell inversion (29). The two fold sets are assigned distinct constitutive responses: the circular folds are bistable, whereas the helical folds remain monostable and approximately linear. The resulting architecture therefore combines local bistability with monotonic axial–transverse coupling.

The second MFT variant employs a fully bistable fold architecture (Fig. 1.C–D) realized through 3D-printed folds composed of thickened members connected by thin, eccentric flexural hinges (see *SI Appendix*, S1). This construction localizes buckling along the prescribed fold trajectories and produces bistability in both the circular and helical fold sets.

Thus, the two MFT variants preserve a common helical–circular fold topology while differing in the distribution of local bistability. The semi-bistable architecture confines bistability to the circular folds, whereas the fully bistable architecture distributes it across both coupled fold sets. This controlled variation isolates how the distribution of local bistability governs the global response.

The BiPlan Modeling Framework

The BiPlan framework, summarized in Fig. 2.A and illustrated for the helical–circular MFT in Figs. 2.B–F, links spatially varying fold geometry and local nonlinear mechanics to global deformation and stability. The MFTs' geometric and mechanical modularity poses two modeling challenges: parameterizing the crease network along the tube and representing bistable constitutive behavior along continuous compliant folds. BiPlan addresses these challenges by mapping the MFT onto a planar domain, decomposing the crease network into characteristic local substructures, and representing compliant folds continuously through bistable planar constitutive fields, termed BiPlan fields.

Unlike lumped hinge or spring models, BiPlan retains the spatial variation of deformation along each continuous compliant fold without introducing independently discretized fold degrees of freedom. The resulting reduced formulation retains fold extension as the leading-order mechanism through which globally dominant axial defor-

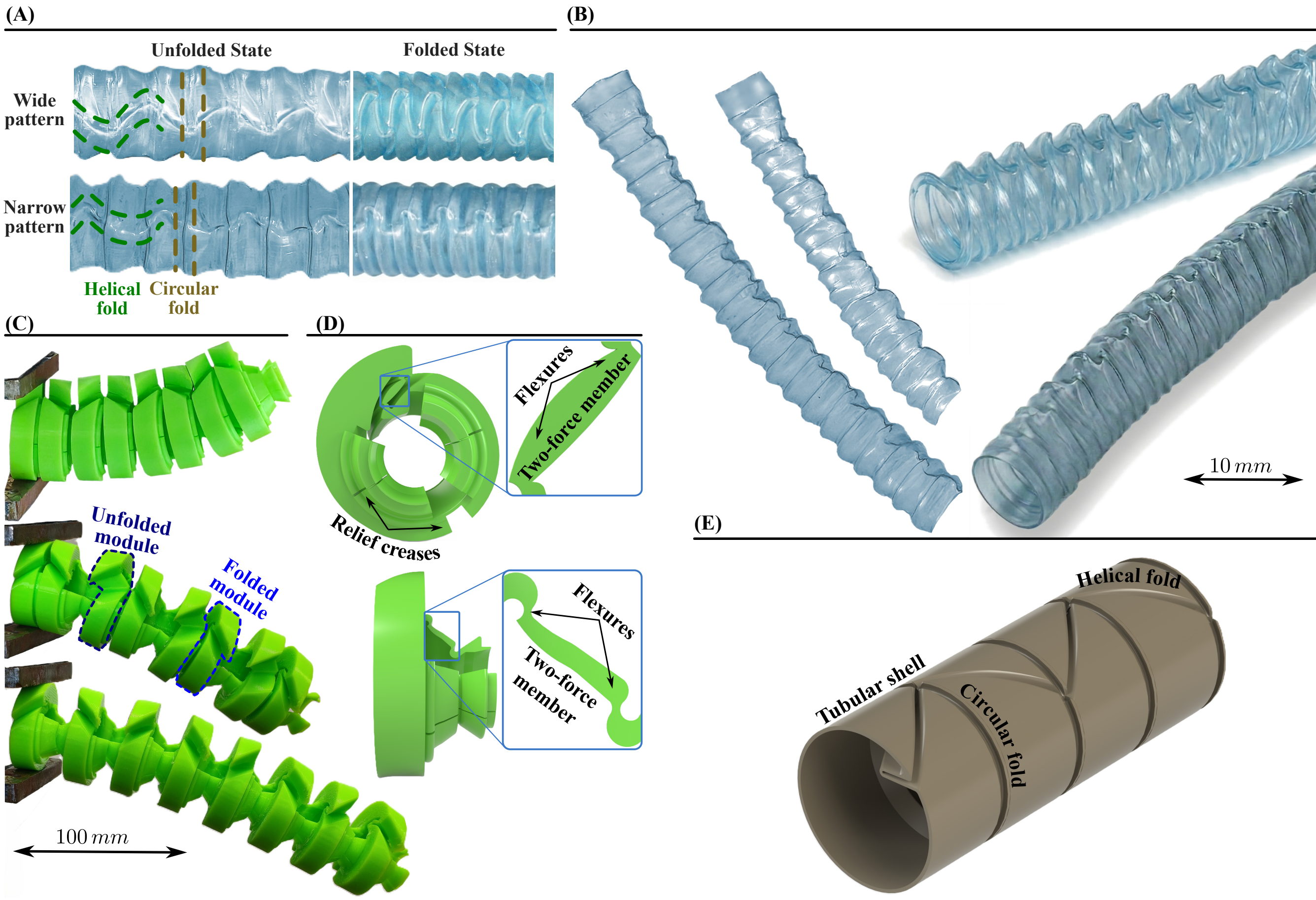

Fig. 1. Two Mixed Folded Tube (MFT) variants sharing a helical–circular crease-network topology but differing in their local fold mechanics. (A) Wide (top) and narrow (bottom) helical geometries shown in unfolded (left) and folded (right) states. Helical and circular fold trajectories are highlighted by green and brown dashed lines, respectively. (B) Corresponding plasticity-induced, semi-bistable MFTs in unfolded and folded configurations. (C) Representative deformation states of a flexure-based, 3D-printed fully bistable MFT, with unfolded and folded modules highlighted. (D) Front (top) and side (bottom) views of a fully bistable MFT unit, with enlarged views of the corresponding bistable fold mechanisms on the right. (E) Schematic of the helical–circular crease network.

mation is accommodated. Accordingly, shell facets are treated as inextensible, fold shear is suppressed through kinematic constraints, and out-of-plane shell bending is neglected. The local field energies are assembled subject to compatibility, guide, and nonpenetration constraints and combined with kinetic energy to determine the dynamic response. Static equilibria are recovered as stationary configurations of the constrained potential, and their local stability is determined from its second variation.

Bistable Planar Constitutive Fields (BiPlan Fields). Within the reduced deformation space defined above, each BiPlan field $\mathcal{S}$ is compliant along its local opening direction and rigid in the transverse direction. Accordingly, a BiPlan field is characterized by its local elongation $w = w(x;\boldsymbol{q})$ determined by the relative rigid-body motion of the adjacent rigid elements, and the piecewise differential stiffness $k_{\mathrm{bi}}(w)$ associated with a trilinear constitutive law:

$$\mathcal{S} = \left[w(x;\boldsymbol{q}),\, k_{\mathrm{bi}}(w)\right], \quad x \in [0, L], \qquad \textbf{[1]}$$

where x is the local coordinate along a fold axis of length L, and $\boldsymbol{q}$ collects the generalized coordinates of the associated substructure (Figs. 2.C–E). The corresponding bistable constitutive relations (Fig. 2.F) exhibit two stable branches separated by an intermediate unstable branch (30):

$$F(w) = \int_0^w k_{\mathrm{bi}}(\xi)\, d\xi, \quad \Psi(w) = \int_0^w F(\xi)\, d\xi, \qquad \textbf{[2]}$$

which, when integrated along the fold axis, yields the strain energy stored in a single BiPlan field:

$$\Pi_{\mathcal{S}} = \int_0^L \Psi\left(w\left(x;\boldsymbol{q}\right)\right)\, dx. \qquad \textbf{[3]}$$

The spatial variation of $w(x;q)$ allows different portions of a single fold to occupy different constitutive branches without introducing independently discretized degrees of freedom along the fold, thus enabling continuous phase transformation.

The field's transverse rigidity is imposed by kinematic guides that constrain normal motion along a single boundary (nodes C, F in Fig. 2.C), while higher-order rotation-induced normal displacements are neglected. The resulting constraints are enforced through guide-axis displacements $\boldsymbol{g}$ with Lagrange multipliers $\boldsymbol{\lambda}$. Additionally, penetration between the connected rigid elements is prevented by constraining the field's boundary elongations to remain nonnegative through unilateral contact conditions (see *SI Appendix*, S2):

$$\mathbf{0} \leq \boldsymbol{w}_{\partial} \perp \boldsymbol{\lambda}_{\partial} \geq \mathbf{0}, \qquad \textbf{[4]}$$

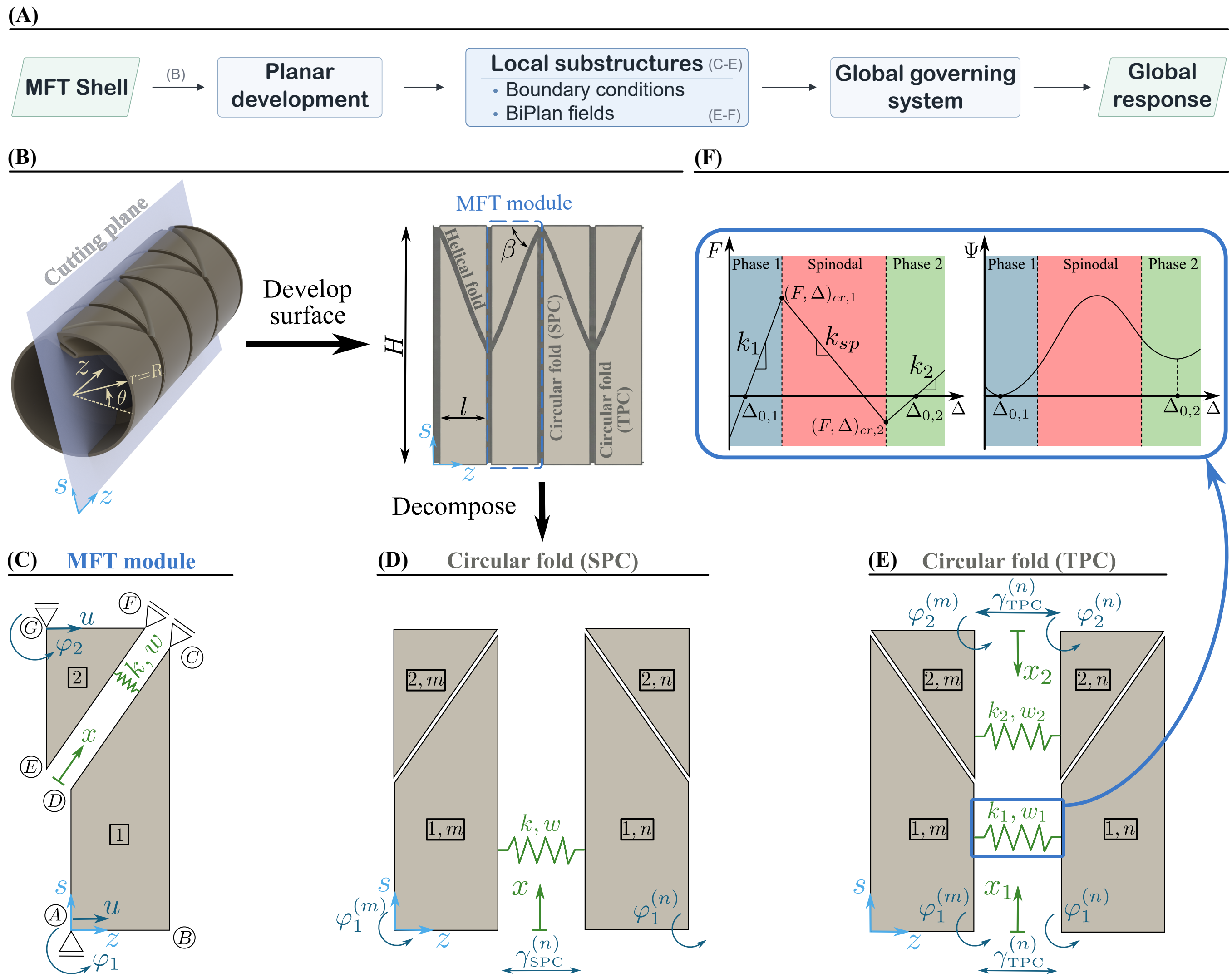

Fig. 2. Modeling mixed folded tubes (MFTs). (A) Schematic of the MFT modeling procedure. Indices refer to the corresponding implementation subpanels. (B-E) Implementation of the model procedure to a representative MFT structure. (B) Planar development of the MFT shell. (C) Basic MFT module, modeled as two rigid elements connected by a helical compliant crease. Kinematic guides constrain normal motion and enforce compatibility. (D-E) Local kinematic schemes for SPC and TPC circular-fold connectors between adjacent MFT modules m and n. (F) Axial crease compliance represented by continuous bistable stiffness fields, approximated by a trilinear differential force law (left) and the corresponding two-well energy density (right).

where $\boldsymbol{w}_\partial$ and $\boldsymbol{\lambda}_\partial$ denote the associated boundary elongations and contact Lagrange multipliers, respectively. Thus, the field energy and its kinematic and unilateral constraints are combined in the augmented potential contribution

$$\Pi_{\mathcal{S},\mathrm{aug}} = \Pi_{\mathcal{S}} + \boldsymbol{\lambda}^{\mathrm{T}}\boldsymbol{g} - \boldsymbol{\lambda}_\partial^{\mathrm{T}}\boldsymbol{w}_\partial. \qquad [5]$$

Equilibrium Stability. The nonlinear fold-energy landscape may admit multiple global equilibria. At an equilibrium $\boldsymbol{q}^*$, local stability is determined by the second variation of the global constrained potential Π_{c} over perturbations that preserve the active constraints $\boldsymbol{c}(\boldsymbol{q}) = \boldsymbol{0}$. Let $\boldsymbol{A} = \partial_{\boldsymbol{q}}\boldsymbol{c}|_{\boldsymbol{q}^*}$ denote the active-constraint Jacobian, and let $\boldsymbol{N}$ span its null space. The reduced Hessian is therefore

$$\boldsymbol{H}_r = \boldsymbol{N}^{\mathrm{T}}\, \partial^2_{\boldsymbol{qq}}\Pi_{\mathrm{c}}\big|_{\boldsymbol{q}^*} \boldsymbol{N}. \qquad [6]$$

An equilibrium is locally stable when $\boldsymbol{H}_r$ is positive definite and loses stability when its smallest eigenvalue reaches zero. The MFT response is classified as monostable, bistable, or multistable according to the number of admissible stable equilibria under the prescribed conditions.

Dynamic Response and Branch Selection. Multistable fold architectures may induce global stability loss, driving the MFT away from its current equilibrium branch. Although stationary energy conditions identify the admissible equilibria, they do not determine the transient trajectory or the branch dynamically reached under a prescribed loading history (31, 32). To resolve this transient evolution and determine the dynamically accessible response branch, BiPlan incorporates the substructure's inertia through the augmented Lagrangian $\mathcal{L}_{\mathrm{aug}} = T - \Pi_{\mathrm{aug}}$.

The corresponding constrained equations of motion are integrated under the prescribed loading history. Following loss of stability, the resulting transient evolution selects the dynamically accessible deformation path and subsequent response branch (see *SI Appendix*, S3–4).

Application to Helical–Circular MFTs. We apply the BiPlan framework to the helical–circular crease topology shared by the semi- and fully bistable MFT variants (Fig. 1), with detailed geometric and kinematic mappings provided in the *SI Appendix*, S2–6. The cylindrical shell of radius R is developed from (z, θ) onto the planar domain (z, s), where $s = R\theta$ (Fig. 2.B). In this domain, the crease network is parameterized by its circumference $H = 2\pi R$, circular-fold pitch l, and helical-fold angle β.

The development is decomposed into local MFT modules, each comprising two rigid elements connected by a helical BiPlan field (Fig. 2.C). The motion of module n is represented by

$$\boldsymbol{q}^{(n)} = \left[u_n,\, \varphi_1^{(n)},\, \varphi_2^{(n)}\right]^{\mathrm{T}}, \qquad [7]$$

where u_n is the common axial translation and $\varphi_i^{(n)}$ is the in-plane rotation of element i. Transverse crease motion is suppressed by kinematic guides, while development compatibility between the corresponding boundaries AB and GF is enforced through the common axial translation u_n and vertical guides. Together, these constraints leave one admissible module degree of freedom (DOF).

Adjacent modules are coupled by circular folds with topology-dependent kinematics (Fig. 2.D–E). A single-pair connector (SPC) comprises a single BiPlan field and forms an open kinematic chain, whereas a two-pair connector (TPC) comprises two parallel fields and forms a closed kinematic loop. The fields' elongations vary with the adjacent modules' rotations, thereby compliantly coupling neighboring modules. The modules' relative rigid-body displacement determines the boundary elongations:

$$\gamma_{\mathrm{SPC}}^{(n)} = w(0), \quad \gamma_{\mathrm{TPC}}^{(n)} = w_1(0) = w_2(0), \qquad [8]$$

where the TPC equality enforces development compatibility between its parallel fields. The MFT is globally constructed by assembling the local generalized coordinates via chain kinematics, enabling the application of global loading and constraints with a global strain energy of

$$\begin{aligned}\Pi_{\mathrm{MFT}} = &\sum_{n=1}^{N} \Pi_{\mathrm{helic}}^{(n)}\left(\boldsymbol{q}^{(n)}\right)\\ &+ \sum_{n=1}^{N} \Pi_{\mathrm{circ}}^{(n)}\left(\boldsymbol{q}^{(n-1,n)}, \gamma^{(n)}\right),\end{aligned} \qquad [9]$$

where $\boldsymbol{q}^{(m,n)}$ collects the coordinates of adjacent modules m and n, with $\boldsymbol{q}^{(0)}$ prescribed by the base boundary conditions. $\gamma^{(n)}$ denotes the connector-specific coordinate, and helical fold and circular connector contributions are Π_{helic} and Π_{circ}, respectively. The corresponding inertial and unilateral contact terms are assembled through the shared coordinates and incorporated into the governing system. The two MFT variants share this formulation but differ in their local constitutive assignments: the semi-bistable variant assigns bistability to the circular folds while maintaining linearity in the helical folds through a single-branch differential constitutive law, whereas the fully bistable variant assigns bistability to both fold sets. This common formulation isolates how the spatial distribution of local bistability within a fixed crease topology governs the global dynamic response and equilibrium stability.

Programmable Deformation and Stability in Semi-Bistable MFTs

Applying the BiPlan formulation, we construct the semi-bistable MFT design space by varying the geometric and constitutive properties of its fold architecture. These properties are parameterized by the fold arc-length and differential stiffness ratios

$$b = \frac{\ell^{\mathrm{helic}}}{\ell^{\mathrm{circ}}}, \quad C = \frac{k^{\mathrm{helic}}}{k_1^{\mathrm{circ}}}, \qquad [10]$$

respectively, where $\ell^{\mathrm{helic}} = l/\cos\beta$ and $\ell^{\mathrm{circ}} = H$. A force-controlled sweep over b and C maps the resulting axial and radial endpoint deformations (Fig. 3.A.1), while a complementary displacement-controlled sweep maps the MFT's stability regimes as functions of the imposed displacement and stiffness ratio C (Fig. 3.A.3). The loading conditions and fixed parameter values used in these sweeps are provided in the *SI Appendix*, S9.

As shown in Fig. 3.A.1, the distinct axial and radial response landscapes show that global MFT deformation can be biased toward axial extension or radial deflection through the geometric and constitutive parameters of its fold architecture. The oblique contours of the axial-displacement map indicate a coupled dependence on b and C, with maximum extension occurring at low values of both parameters. In contrast, radial displacement decreases from a maximum at low b and C toward a minimum at high C and intermediate b, where radial deformation is most strongly suppressed.

To further examine the predicted MFT response and validate the BiPlan model, we select a representative design marked by the star in Fig. 3.A.1 and compare its force–displacement response with measurements from pneumatically actuated MFT specimens (Fig. 3.A.2 and Movie S1). The constitutive laws assigned to the circular and helical BiPlan fields were identified independently using measurements from separate Circular Folded Tube specimens (*SI Appendix*, S10), so the assembled MFT measurements provide an independent validation of the global model response. The prediction agrees well with the experimental measurements, remaining within the ± 1 standard-deviation band over most of the deformation range, with a slight overprediction of the initial stiffness. BiPlan also captures the overall response sequence, comprising a transition between two stable phases through an intermediate spinodal regime characterized by a loss of global tangent stiffness. To examine the deformation modes associated with each regime, we consider representative states marked along the response curve and shown in Fig. 3.B.

The simulated and experimental configurations exhibit consistent phase-dependent deformation modes. During the initial phase, axial loading extends the linear helical folds together with the bistable circular folds, while the latter remain predominantly in their first stable state. Coupling through the inclined helical folds causes the circular folds to extend and transition nonuniformly

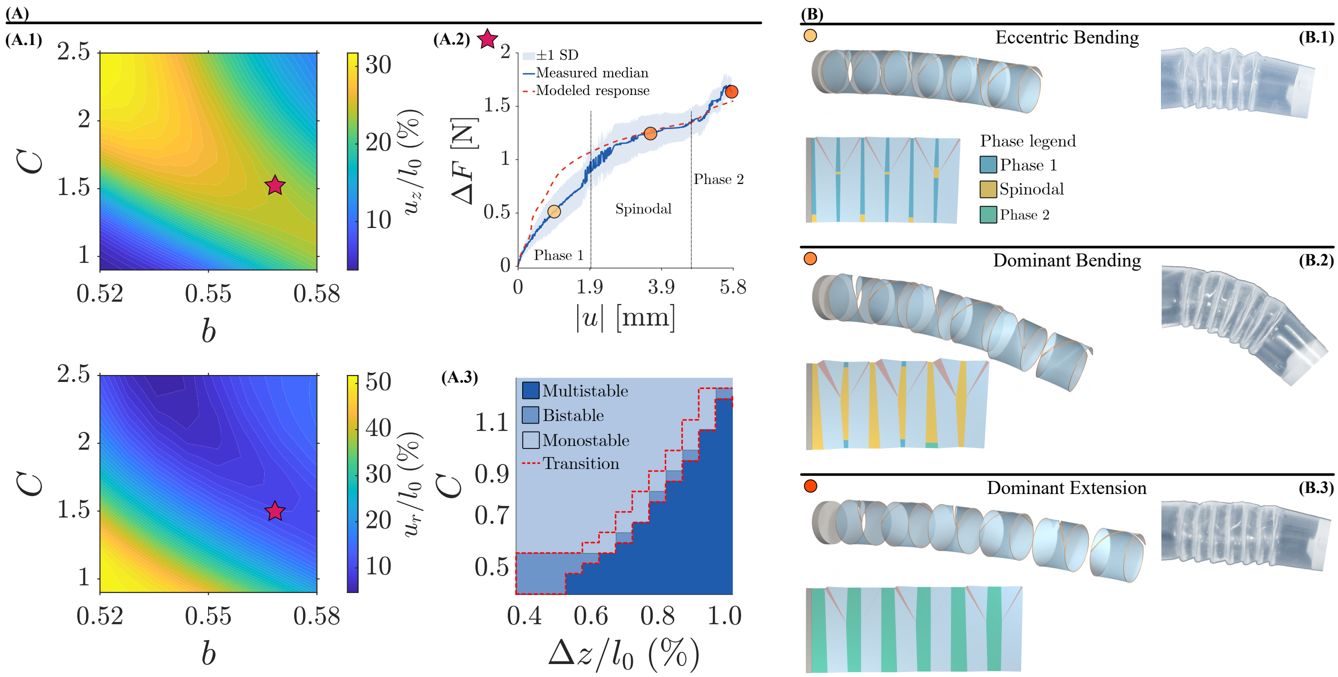

Fig. 3. Design-space prediction and experimental validation of a semi-bistable MFT. (A.1) Predicted axial and radial endpoint displacements, u_z (top) and u_r (bottom), normalized by the initial MFT length l_0, across the (b, C) design plane under a monotonic axial-force ramp to $F_f = 1.6$ N. A star marks the experimentally validated design. (A.2) Predicted force–displacement response compared with the measured median and shaded ± 1 SD band across five semi-bistable MFT specimens. (A.3) Stability map at $b = 0.58$ as a function of normalized axial displacement and C, showing mono-, bi-, and multistable regions and the intervening transition region. (B.1–B.3) Representative simulated and experimental configurations in Phase 1, the spinodal regime, and Phase 2, respectively. For each state, the simulated cylindrical reconstruction and planar development are shown on the left, while the corresponding experimental configuration is shown on the right.

along the circumference, driving global eccentric bending (Fig. 3.B.1). As a sufficiently large portion of the circular folds enters the spinodal branch, the MFT is driven to global instability, and bending becomes the dominant deformation mode as the circumferential stiffness becomes increasingly nonuniform (Fig. 3.B.2). Further axial loading completes the transition of the circular folds into their second stable, unfolded state, restoring a globally stable response characterized by dominant extension (Fig. 3.B.3).

Complementing the force-controlled characterization and model validation, a quasi-static displacement-controlled analysis maps the stability regimes as functions of the imposed displacement and stiffness ratio C (Fig. 3.A.3). The map reveals an overall transition from monostability at smaller displacements and higher stiffness ratios to multistability at larger displacements and lower stiffness ratios. These regimes are separated by an intermediate transition region in which the predicted response alternates between bistable and multistable solutions.

Together, the force- and displacement-controlled maps show that the semi-bistable fold architecture can be tuned to program both endpoint deformation and the number of stable global equilibria. Because bistability is confined to the circular folds, coupling to the monostable helical folds distributes the phase transformation along the tube, producing a compliant deformation path whose axial and transverse components can be tuned through local fold geometry and stiffness contrast.

Hierarchical State Space and Transition Pathways in Fully Bistable MFTs

Extending bistability from the circular folds to both coupled fold sets shifts the global response from the distributed phase transformation of the semi-bistable MFT to transitions among discrete stable configurations. Because neighboring modules are kinematically coupled, the state of one fold constrains the deformations compatible with the remainder of the sequence. The resulting stable equilibria form a transition network in which ordered sequences of discrete transitions define pathways between selected initial and target configurations.

Using BiPlan, we map the stable equilibria of a four-module fully bistable MFT and construct a transition diagram based on single-fold state adjacency (Fig. 4.A; *SI Appendix*, S11). Each node represents a predicted stable equilibrium, while an edge connects two configurations that differ in the state of a single fold. An ordered sequence of connected states defines a deformation pathway between selected initial and target configurations. Projecting the stable equilibria and pathways into endpoint-configuration space, parameterized by elongation u_z, deflection u_r, and slope θ (Fig. 4.B), reveals a hierarchical distribution of stable states across this space (Fig. 4.C). Three representative pathways, highlighted in both the transition diagram and endpoint-configuration space, are reproduced experimentally (Fig. 4.A–B,D).

Projecting the stable equilibria into endpoint-configuration space reveals a three-level hierarchy arising from the coupling between the bistable fold states and the MFT chain kinematics (Fig. 4.B–C; *SI Appendix*, S12). At the first level, the number of open helical folds sets the accumulated module rotation and therefore determines

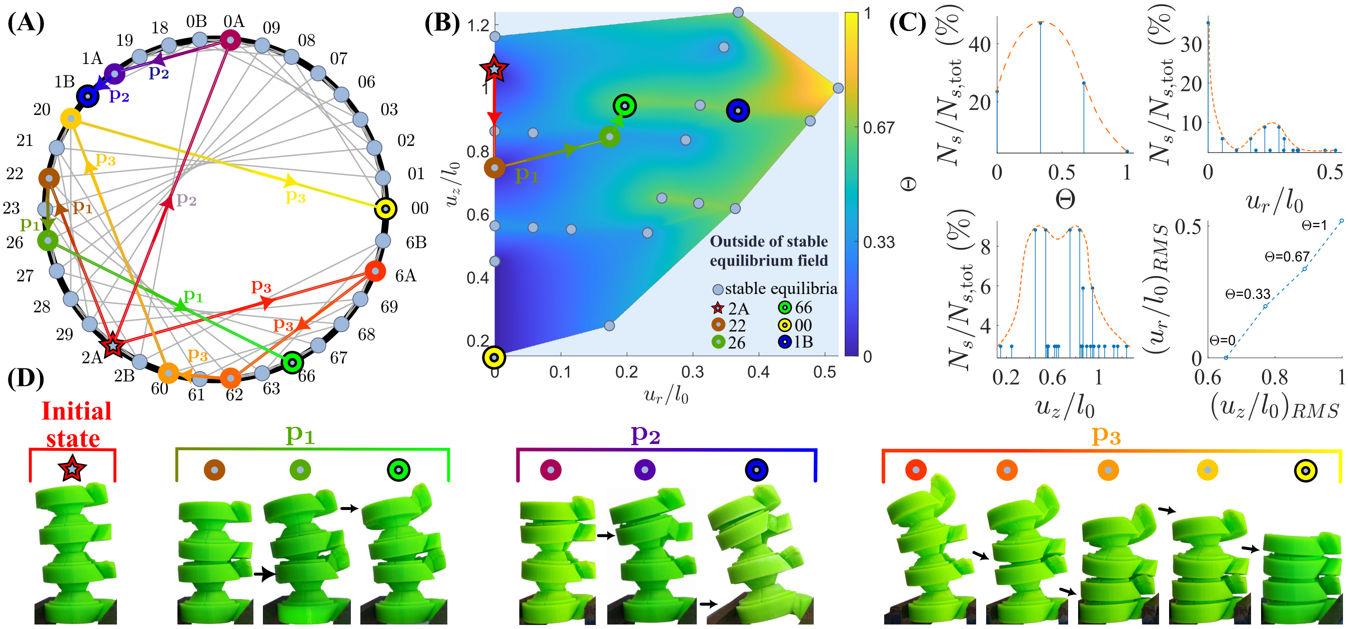

Fig. 4. Stable-state landscape of a four-module fully bistable MFT. (A) State-transition diagram constructed from single-fold state adjacency. Blue nodes denote predicted stable equilibria and are labeled by two-digit hexadecimal representations of seven-bit fold-state sequences ordered from the MFT's free end toward its clamped base, with closed and open folds denoted by 0 and 1, respectively. A leading zero is appended before hexadecimal conversion. Gray edges connect configurations whose fold-state sequences differ by a single bit, and colored sequences indicate three experimentally realized deformation pathways. (B) Projection of the stable equilibria into endpoint-configuration space, parametrized by axial and radial endpoint displacements, u_z and u_r, respectively, normalized by the compressed MFT length l_0, and normalized endpoint slope $\Theta = \theta/\max|\theta|$. p_1 and target states of $p_{2,3}$ are marked. (C) state-count distributions over endpoint slope, elongation, and deflection, together with the corresponding branchwise RMS relations. (D) Experimental realizations of the three highlighted deformation pathways. Arrows indicate a fold state change between successive configurations.

discrete, equally spaced endpoint-slope branches. Within each slope branch, the circular-fold configuration controls intermodule extension and partitions the states into iso-elongation subbranches. The axial positions of the open helical folds then govern deflection within each subbranch: opening a fold closer to the clamped base rotates a longer downstream portion of the MFT and therefore produces a larger endpoint deflection. Across these hierarchical levels, elongation and deflection also vary systematically with slope, as branchwise RMS averaging shows that they increase approximately linearly with endpoint slope. Thus, helical-fold count, circular-fold configuration, and helical-fold position organize the stable states into a coupled hierarchy in which local fold states successively govern the slope, elongation, and deflection of the global configuration.

The realized pathways demonstrate how this hierarchical state space can be navigated. Beginning from the common initial state 2A, pathways p_1 and p_2 terminate at states 66 and 1B, respectively. These target states occupy the iso-elongation subbranch $u_z/l_0 = 0.9$ within the $\Theta = 0.67$ endpoint-slope branch, while exhibiting distinct deflections, consistent with the different axial positions of their open helical folds. Pathway p_3, by contrast, reaches the fully contracted state 00, in a different region of the state space. The experiments therefore establish the physical accessibility of selected routes through the state-adjacency graph and show that local fold-switching sequences program both the target configuration and the pathway by which it is reached.

Concluding Remarks

In this work, we expanded the design space of origami-inspired structures by introducing localized instabilities within the folds, thereby creating Mixed Folded Tubes (MFTs), compliant multistable structures whose local fold architectures govern global deformation and stability through both constitutive mechanics and geometric constraints.

BiPlan captures this local-to-global coupling by representing compliant folds through continuous fields that capture spatially varying bistable mechanics, relating local fold geometry and mechanics to global equilibrium configurations, their stability, and the dynamically accessible response following stability loss. For semi-bistable MFTs, the framework predicts the force–displacement response and phase-dependent deformation modes observed in pneumatic experiments. For fully bistable MFTs, BiPlan maps the stable equilibrium states and the transition pathways connecting them, with representative predicted pathways reproduced experimentally.

The design maps demonstrate that global deformation and stability can be programmed through the local geometric and mechanical parameters of the fold architecture, while the controlled comparison between architectures with a common crease-network topology reveals how the distribution of local bistability changes the character of the global response. Restricting bistability to a subset of folds permits compliant deformation through a spatially distributed phase transformation, whereas distributing bistability across coupled folds produces discrete transitions among hierarchically organized stable configurations. Together, these results establish local fold architecture, combining crease-network geometry with local nonlinear mechanics, as a basis for programming both the stable configurations of a structure and the transition pathways connecting them, thereby expanding the realizable morphing landscape for multistable metamaterials, adaptive structures, and soft robotic systems.

Data, Materials, and Software Availability. All data and code supporting the findings of this study will be made publicly available on GitHub and archived in Zenodo upon publication. During peer review, these materials are available from the corresponding author upon request.

1. RL Harne, KW Wang, *Harnessing bistable structural dynamics: for vibration control, energy harvesting and sensing.* (John Wiley & Sons), (2017).
2. Y Cao, M Derakhshani, Y Fang, G Huang, C Cao, Bistable structures for advanced functional systems. *Adv. Funct. Mater.* **31**, 2106231 (2021).
3. C De Castro, D Orlando, P Gonçalves, Nonlinear dynamics of elastically connected multistable structures in *Journal of Physics: Conference Series.* (IOP Publishing), Vol. 2647, p. 092001 (2024).
4. B Gorissen, D Melancon, N Vasios, M Torbati, K Bertoldi, Inflatable soft jumper inspired by shell snapping. *Sci. Robotics* **5**, eabb1967 (2020).
5. J Tirado, CD Do, J Moisson de Vaux, J Jørgensen, A Rafsanjani, Earthworm-inspired soft skin crawling robot. *Adv. Sci.* **11**, 2400012 (2024).
6. C Aza, A Pirrera, M Schenk, Multistable morphing mechanisms of nonlinear springs. *J. Mech. Robotics* **11**, 051014 (2019).
7. Y Chi, et al., Bistable and multistable actuators for soft robots: Structures, materials, and functionalities. *Adv. Mater.* **34**, 2110384 (2022).
8. D Rus, MT Tolley, Design, fabrication and control of soft robots. *Nature* **521**, 467–475 (2015).
9. P Polygerinos, et al., Soft robotics: Review of fluid-driven intrinsically soft devices; manufacturing, sensing, control, and applications in human-robot interaction. *Adv. engineering materials* **19**, 1700016 (2017).
10. X Tang, et al., A review of soft actuator motion: Design, manufacturing and applications. *Actuators* **11** (2022).
11. S Li, DM Vogt, D Rus, RJ Wood, Fluid-driven origami-inspired artificial muscles. *Proc. Natl. academy Sci.* **114**, 13132–13137 (2017).
12. P Breitman, et al., Flows in straws: Viscous flows in one-dimensional metamaterial. *Phys. Rev. Appl.* **18**, 064077 (2022).
13. O Peretz, E Ben Abu, A Zigelman, S Givli, AD Gat, A metafluid with multistable density and internal energy states. *Nat. Commun.* **13**, 1810 (2022).
14. J Hua, Y Zhou, CQ Chen, Design and analysis of a tunable multistable mechanical metamaterial. *Int. J. Mech. Sci.* **272**, 109170 (2024).
15. M Schenk, SD Guest, Geometry of miura-folded metamaterials. *Proc. Natl. Acad. Sci.* **110**, 3276–3281 (2013).
16. ET Filipov, GH Paulino, T Tachi, Origami tubes with reconfigurable polygonal cross-sections. *Proc. Royal Soc. A: Math. Phys. Eng. Sci.* **472**, 20150607 (2016).
17. X Yue, M Zhu, H Geng, L Gong, Y Wang, Origami metamaterials and their applications and prospects in the field of aerospace. *Acta Aeronaut. et Astronaut. Sinica* (2025) Early access; in Chinese with English abstract.
18. SD Guest, S Pellegrino, The folding of triangulated cylinders, part i: Geometric considerations. *J. Appl. Mech.* (1994).
19. N Kidambi, K Wang, Dynamics of kresling origami deployment. *Phys. Rev. E* **101**, 063003 (2020).
20. V Brunck, F Lechenault, A Reid, M Adda-Bedia, Elastic theory of origami-based metamaterials. *Phys. Rev. E* **93**, 033005 (2016).
21. SW Grey, F Scarpa, M Schenk, Mechanics of paper-folded origami: A cautionary tale. *Mech. Res. Commun.* **107**, 103540 (2020).
22. A Sharma, S Naskar, T Mukhopadhyay, Programmable constitutive mode-coupling in tubular origami metamaterials. *npj Metamaterials* **1**, 4 (2025).
23. KT Liu, T Tachi, GH Paulino, Actuation driven pseudocrease mechanics in multistable curved-crease origami shells. *Proc. Natl. Acad. Sci.* **123**, e2530458123 (2026).
24. B Zhang, "Bistable and multi-stable thin-walled structures," PhD thesis, University of Oxford (2017).
25. NP Bende, et al., Geometrically controlled snapping transitions in shells with curved creases. *Proc. Natl. Acad. Sci.* **112**, 11175–11180 (2015).
26. Z Wo, ET Filipov, Bending stability of corrugated tubes with anisotropic frustum shells. *J. Appl. Mech.* **89**, 041005 (2022).
27. Y Zhu, ET Filipov, A bar and hinge model for simulating bistability in origami structures with compliant creases. *J. Mech. Robotics* **12**, 021110 (2020).
28. E Filipov, K Liu, T Tachi, M Schenk, GH Paulino, Bar and hinge models for scalable analysis of origami. *Int. J. Solids Struct.* **124**, 26–45 (2017).
29. E Ben-Abu, et al., Directed instability as a mechanism for fabricating multistable twisting microstructure. *Adv. Eng. Mater.* **26**, 2400070 (2024).
30. G Puglisi, L Truskinovsky, Mechanics of a discrete chain with bi-stable elements. *J. Mech. Phys. Solids* **48**, 1–27 (2000).
31. J Thompson, Basic principles in the general theory of elastic stability. *J. Mech. Phys. Solids* **11**, 13–20 (1963).
32. D Shilkrut, About the ways of stability loss by snap-through of geometrically non-linear shells (systems) and some related problems. *Int. journal non-linear mechanics* **29**, 671–686 (1994).